# Investigation of Millimeter-Wave Scattering from Frequency Selective Surfaces

Thomas R. Schimert, *Associate Member, IEEE*, Austin J. Brouns, *Senior Member, IEEE*, Chi H. Chan, *Member, IEEE*, and Raj Mittra, *Fellow, IEEE*

*Abstract*—**A comparative numerical and experimental analysis of scattering from dielectric-backed frequency selective surfaces in W-band (75–110 GHz) has been carried out. The examples studied include metal (aluminum), resistive (bismuth), and bismuth-loaded I-pole or "linearized" Jerusalem cross arrays on fused silica, all of which exhibit a band-stop resonance in W-band as a general feature. The arrays were fabricated using standard photolithographic techniques. The numerical analysis involves the solution of an electric field integral equation using subdomain "rooftop" basis and testing functions within the framework of the Galerkin testing procedure. The lossy nature of the materials has been fully accounted for. A comparative analysis of doubly stacked aluminum I-pole arrays was also carried out. The numerical analysis exploits a variant of the cascade method in that the immediately adjacent dielectric layers are included in the construction of the scattering matrix for the frequency selective surface. This allows the higher order evanescent Floquet modes to sufficiently decay at the dielectric boundaries so they can be ignored in the scattering matrix.**

## I. Introduction

OVER the years, thin periodic arrays serving as frequency selective surfaces (FSS's) have been widely used for a number of millimeter- and submillimeter-wave applications. These include filters [1]–[3], laser cavity output couplers [4]–[6], polarization diplexers [7], spectral diplexers [8], interferometers [9], detectors [10], and, more recently, phase shifters [11], [12] and frequency doublers [13]. In most cases, the FSS is mounted on one or more supporting dielectric layers and in some cases, several FSS's are cascaded together to achieve the desired spectral response [1], [2], [6], [8], [9]. In this paper, the frequency selective properties of a number of I-pole or "linearized" Jerusalem cross type arrays are investigated for use in W band (75–110 GHz). The purpose of the investigation is a comparative study of numerical and experimental results for the various arrays. Results for single dielectric-backed arrays and double arrays in a cascaded configuration are presented. The examples considered include a metal (aluminum) I-pole array, a resistive (bismuth) I-pole array, and a bismuth-loaded aluminum I-pole array, all on fused silica. An example involving doubly stacked aluminum I-pole arrays on fused silica is discussed. An I-pole array has the advantage over a standard dipole array (with dipoles of the same length) in that the resonance position occurs further from the diffraction edge. This reduces any undesirable effects that the diffraction edge might have on the frequency selective properties.

The numerical method used here to describe scattering from a dielectric-mounted FSS has been described elsewhere [14], [15]. The most general dielectric configuration involves an FSS sandwiched between (lossy) dielectric layers together with a lossless superstrate and (lossy) substrate. The method involves solving an electric field integral equation (EFIE) for the current distribution on the FSS and employs rooftop subdomain basis [16], [17] and testing [18] functions within the framework of the Galerkin testing procedure [15]. The method applies to the case of real, i.e., lossy and/or reactive, materials through the use of a complex sheet conductance to describe the FSS. In general, multiple materials can be used as, for example, in the case of a resistive-loaded metal dipole array. The resulting operator equation may be solved iteratively using, for example, the conjugate gradient method (CGM) [17], [19] or solved directly using matrix inversion [16], [20].

The description of scattering from stacked FSS's has been addressed using the cascade approach [15], [21], [22]. In the approach described in these works, a separate scattering matrix is constructed for each FSS and each dielectric layer. A composite scattering matrix for the stack is then formed by a matrix product. For example, the response of an FSS mounted on a dielectric half-space is obtained by cascading the scattering matrix of the free-standing FSS with that for the dielectric interface in the limit where the separation between the FSS and the half-space interface goes to zero. The method, however, has been found [15], [23] to yield incorrect results when used to calculate the resonance of a dipole array on a dielectric half-space unless a prohibitively large number of Floquet modes are retained in the scattering matrix. This is because in the limit of zero spacing between the dielectric interface and the dipole array, the higher order evanescent Floquet mode amplitudes do not decay and hence cannot be ignored when implementing the cascade connection. Because of this, the cascade connection has limited usefulness in any stack configuration which involves cascading freestanding FSS's with immediately adjacent layers, particularly when the dielectric constants are large.

A variation of the cascade connection is described in this paper. It is found to be useful for cascading multiple FSS's in the presence of dielectric layers. The method involves calculating the scattering matrix for the FSS in the presence of the immediately adjacent dielectric layers on either side of the FSS [14], [15]. Inclusion of these dielectric layers allows higher order evanescent Floquet modes to decay sufficiently

Manuscript received January 30, 1990; revised August 27, 1990.

T. R. Schimert and A. J. Brouns are with the LTV Missiles and Electronics Group, P.O. Box 650003, Dallas, TX 75265-0003.

C. H. Chan and R. Mittra are with the Electromagnetic Communication Laboratory, University of Illinois, Urbana, IL 61801.

IEEE Log Number 9041463.

0018-9480/91/0200-0315$01.00 ©1991 IEEE

at the dielectric interfaces so they can be safely ignored when constructing the scattering matrix for the FSS. For given dielectric layer thicknesses, it can be determined *a priori* which of the lower order evanescent Floquet modes have not sufficiently decayed at the dielectric interfaces and must thus be included in the cascade connection.

We remark that other general theories describing scattering from stacked FSS's in the presence of dielectric layers have been discussed [24], [25]. In these theories, the stacked configuration is treated in a single formulation involving a single set of equations which describes the interactions between all the elements in the stack. This is in contrast to the cascade approach used here. Also, single FSS scattering in the presence of multiple dielectric layers has been discussed [26].

## II. Mathematical Preliminaries

The mathematical formulation of scattering from a dielectric-mounted FSS and a derivation of the EFIE for the current distribution on the FSS have been described elsewhere [14], [15] and are briefly reviewed in this section. We then discuss the scattering matrix for an FSS in the presence of immediately adjacent dielectric layers.

The dielectric configuration in Fig. 1 shows an FSS between (lossy) dielectric layers that have complex permittivities, $\tilde{\epsilon}_{l1}$ and $\tilde{\epsilon}_{l2}$, and thicknesses $d_1$ and $d_2$, respectively. There is in addition a (lossy) substrate $\tilde{\epsilon}_{s_2}$, and lossless superstrate $\epsilon_{s_1}$. Fig. 2 shows the geometry of the periodic surface with periodicities $t_x$ and $t_y$ in an orthogonal $x-y$ coordinate system. In this coordinate system the wave vector components are defined as follows:

$$\vec{k}_{0t}^{\,I} = \hat{x}k_x^I + \hat{y}k_y^I \tag{1a}$$

$$k_x^I = k_0^I \sin\theta^I \cos\phi^I \tag{1b}$$

$$k_y^I = k_0^I \sin\theta^I \sin\phi^I \tag{1c}$$

$$k_{xm} = \frac{2\pi m}{t_x} + k_x^I \tag{1d}$$

$$k_{yn} = \frac{2\pi n}{t_y} + k_y^I \tag{1e}$$

$$\gamma_{l_i(s_i)mn} = \pm j\left(\tilde{\epsilon}_{l_i(s_i)}\omega^2/c^2 - k_{xm}^2 - k_{yn}^2\right)^{1/2}, \qquad i=1,2 \tag{1f}$$

with $k_0^I = \sqrt{\epsilon_{s_1}}\,\omega/c$. $\vec{k}_{0t}^{\,I}$ is the transverse (to $z$) component of the incident wave vector; $k_{xm}$ and $k_{yn}$ are the transverse components of the $(m,n)$ Floquet mode wave vector; and $\gamma_{l_i(s_i)mn}$ is the $z$ component for the $(m,n)$ mode in the $l_i(s_i)$ layer, $i=1,2$. The $+(-)$ sign in (1f) is used when the real part of the square root argument is positive (negative), corresponding to a propagating (evanescent) mode.

The EFIE to be solved [14], [15] can be written in the operator form

$$-\vec{E}^I = \overleftrightarrow{G} * \vec{J} - \frac{1}{\sigma_{ss}}\vec{J} \tag{2}$$

where $\vec{E}^I$ is the incident excitation field, $\overleftrightarrow{G}$ is the relevant Green's function for the dielectric configuration described in Fig. 1, $\vec{J}$ is the unknown surface current, and $\sigma_{ss}$ is the complex sheet conductance for the FSS describing its ohmic properties. As will be shown in Section IV, this term is

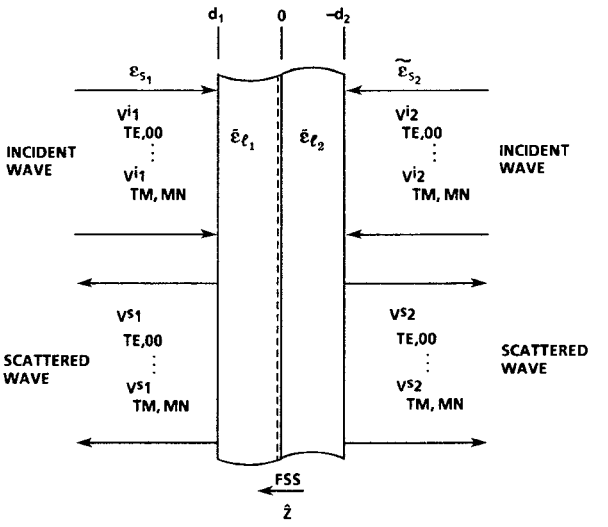


Fig. 1. Description of an FSS in the presence of dielectric layers. Also shown are the incident and scattered voltage waves used in the scattering matrix construction.

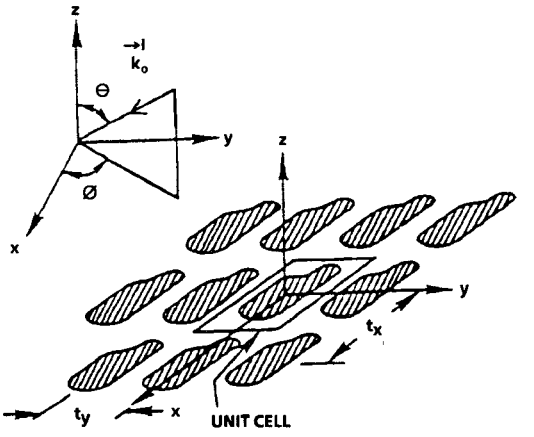


Fig. 2. Geometry of a periodic surface.

important not only in the resistive and resistive-loaded I-pole arrays but also for the aluminum I-pole array. In solving (2), we have employed rooftop subdomain basis and testing functions within the framework of the Galerkin testing procedure [15]. For the results presented herein, (2) was solved iteratively using the conjugate gradient method [17], [19].

We now turn to a discussion of the cascade connection for a stack of dielectric-supported FSS's and the construction of the scattering matrix for an FSS in the presence of the immediately adjacent dielectric layers. The cascade method used here is a variant of that described in [15], [21], and [22]. In these works, the scattering matrix for an FSS/dielectric stack is constructed by cascading the scattering matrices of the freestanding FSS's together with the supporting dielectric layers. As remarked previously, this method has been found to yield incorrect results unless a prohibitively large number of Floquet modes are retained in the scattering matrix [15], [23]. In the method used here, the scattering matrix for the freestanding FSS is replaced with that of the FSS together with the immediately adjacent dielectric layers, i.e., the layers denoted by $l_1$ and $l_2$ in Fig. 1. In this way, higher order evanescent Floquet modes are vanishingly small

at the dielectric boundaries $z = d_1$ and $-d_2$, and do not contribute to the cascade connection. Furthermore, owing to the $\exp(-|\gamma_{l_i}|z)$ dependence in the evanescent modes, it can be determined for given layer thicknesses which modes need to be retained in the scattering matrix for the FSS. The method retains most of the versatility of the original method in that, once solved for, the scattering matrix for the composite FSS/adjacent layers structure can be used to analyze a FSS stack in various configurations, e.g., different layer configurations, provided the layers adjacent to the FSS remain unchanged.

For an FSS sandwiched between dielectric layers, the scattering matrix $\overleftrightarrow{S}$ relating the incident Floquet voltage waves $\vec{V}^i$ to the scattered Floquet voltage waves $\vec{V}^s$ is defined in the usual manner [15], [21], [22]:

$$\vec{V}^s = \overleftrightarrow{S}\vec{V}^i. \tag{3}$$

Referring to Fig. 1, (3) can be written as

$$\begin{bmatrix} \vec{V}^{s_1} \\ \vec{V}^{s_2} \end{bmatrix} = \overleftrightarrow{S} \begin{bmatrix} \vec{V}^{i_1} \\ \vec{V}^{i_2} \end{bmatrix} \tag{4a}$$

with

$$\overleftrightarrow{S} = \begin{bmatrix} \overleftrightarrow{R}_{11} & \overleftrightarrow{T}_{12} \\ \overleftrightarrow{T}_{21} & \overleftrightarrow{R}_{22} \end{bmatrix} \tag{4b}$$

and

$$\vec{V}^{s_1} = \begin{bmatrix} V^{s_1}_{\mathrm{TE},00} \\ \vdots \\ V^{s_1}_{\mathrm{TM},mn} \end{bmatrix}, \text{ etc.} \tag{4c}$$

The $\overleftrightarrow{R}_{11}$ and $\overleftrightarrow{T}_{21}$ submatrices contain the reflection and transmission coefficients for the incident field on the FSS from the left in Fig. 1. Similarly $\overleftrightarrow{R}_{22}$ and $\overleftrightarrow{T}_{12}$ contain the reflection and transmission coefficients for the incident field from the right. In general, $\overleftrightarrow{R}_{11} \neq \overleftrightarrow{R}_{22}$ and $\overleftrightarrow{T}_{12} \neq \overleftrightarrow{T}_{21}$, as was the case for the freestanding FSS because the dielectric layers on either side of the FSS are, in general, different. The derivation of the $\overleftrightarrow{R}_{ij}$ and $\overleftrightarrow{T}_{ij}$ follows that outlined in [15].

## III. Fabrication and Testing of Arrays

Photographs of an aluminum and a bismuth-loaded aluminum array are shown in Fig. 3. The arrays were fabricated on 25-mm-diameter by 0.82-mm-thick fused silica substrates of dielectric constant 3.8. Contact photolithography was employed utilizing a Suss MJB3 mask aligner with 320 nm wavelength exposure, an image reversal resist (AZ-5214), and a lift-off procedure. The bismuth-loaded aluminum array in Fig. 3(b) required a two-step process involving the deposition of center-gapped aluminum I-poles followed by deposition of the bismuth loads. Measured I-pole dimensions are given in the first column of Table I. The vertical and horizontal periodicities are $t_y = 1.02$ mm and $t_x = 0.88$ mm. The all-bismuth array appears similar to the aluminum array.

Transmittance measurements were made (with electric field parallel to the I-pole) using a Hewlett-Packard Model 8510B vector network analyzer with a millimeter-wave source module and mixers covering the frequency range 75–100 GHz. The test arrays were mounted in a 22 mm aperture in an opaque baffle covered by millimeter-wave-absorbent material. The separation between the transmitting and receiving horns was 61 cm. A simple response calibration was performed. The response reference was established by measuring the transmittance through the open aperture. Phase measurements were made only on the aluminum I-pole array. A phase reference was established by measuring the transmission phase through the array with the I-poles oriented transverse to the incident electric field. Error-free reflectance measurements were not possible in the test environment, so the absorption of the test articles could not be derived.

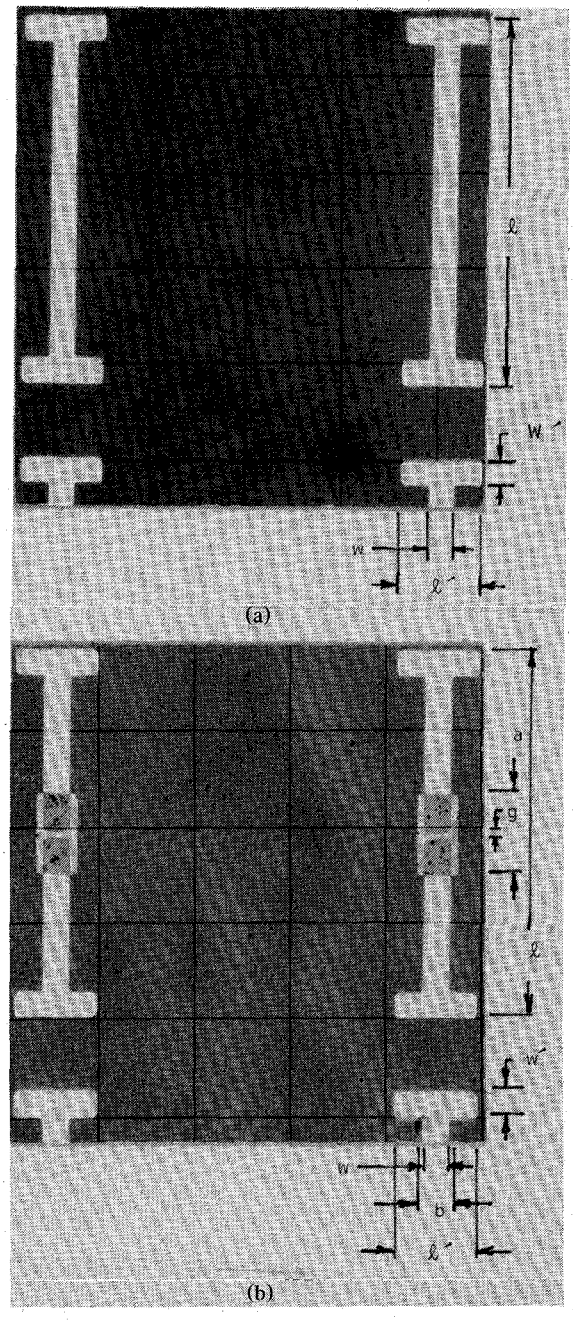


Fig. 3. (a) Aluminum and (b) bismuth-loaded aluminum I-pole arrays with dimensions given in Table I.

TABLE I
DIMENSIONS FOR THE I-POLE ARRAYS COMPARED WITH THE MODELED DIMENSIONS (NUMBER OF RESOLUTION ELEMENTS SHOWN IN PARENTHESES)

| Dimensions | Measured (mm) | 52×54 Grid (mm) | 28×24 Grid (mm) Case 1 | 28×24 Grid (mm) Case 2 |
|---|---|---|---|---|
| $l$ | 0.85 | 0.85 (45) | 0.85 (20) | 0.85 (20) |
| $w$ | 0.058 | 0.051 (3) | 0.063 (2) | 0.063 (2) |
| $w'$ | 0.048 | 0.056 (3) | 0.042 (1) | 0.085 (2) |
| $l'$ | 0.188 | 0.187 (11) | 0.189 (6) | 0.189 (6) |
| $g$ | 0.036 | 0.038 (2) | | |
| $a$ | 0.193 | 0.188 (10) | | |
| $b$ | 0.099 | 0.085 (5) | | |

## IV. RESULTS

For the numerical analysis, the complex sheet conductances of the metal films were derived from dc resistance measurements. The dc conductivity of the 1800 Å aluminum I-pole film was $1.8\times10^5$ $(\Omega\cdot\text{cm})^{-1}$, about half that of pure bulk aluminum. For metals at millimeter and longer wavelengths ($f < 300$ GHz), the imaginary part of the complex conductivity is small while the real part can be approximated by the dc conductivity [27]:

$$\hat{\sigma} = \sigma_1 + j\sigma_2 \sim \sigma_1 \sim \sigma_{\text{dc}}.$$

Applying the relation $\hat{\sigma} = \omega\epsilon_0\,[2NK + j(N^2 - K^2)]$, the refractive indexes of the film are found to be $N \sim K \sim 1300$. The corresponding skin depth is 4100 Å. Applying the procedure described in the Appendix, an effective sheet conductance of $\hat{\sigma}_{ss} = 3.0 - j.08$ $(\Omega/\text{square})^{-1}$ was obtained for the aluminum I-poles. In Fig. 4, the measured transmittance of the aluminum I-pole array is compared with predicted values for various modeling parameters. The array is resonant at 91 GHz, exhibiting a band-stop response in transmittance.

In the numerical analysis, a trade-off is involved in selecting the number of resolution elements (per unit cell) used to model the array dimensions. Increasing the resolution provides a more accurate representation but may lead to excessive computation times.

The results for a $52\times54$ $(x-y)$ grid in Fig. 4(a) are in excellent agreement with the experimental transmittance, both in the position and in the width of the band-stop resonance. Using such a large grid allows all the modeled I-pole dimensions to correlate well with the measured values, as shown in Table I. Results for a smaller, $28\times24$, grid are also presented for two cases in Table I. The I-pole width parameters $w$ and $w'$ are not accurately modeled in either case. In case 1, the modeled value for $w$ is 13% larger than measured and $w'$ is 8% smaller, resulting in a predicted resonance shift to 94 GHz. However, in case 2, where $w'$ has been doubled and is now 34% larger than measured, the agreement is again excellent.

This example illustrates the advantage of high grid resolution when modeling FSS's with complex resonant elements. The larger grid size, however, is considerably more computationally intensive. For example, the $52\times54$ grid solution took an average of 150 iterations to converge to less than 1% error, while the $28\times24$ grid solution in case 2 took an average of only 45 iterations. In light of this, considerable computation time can be saved in FSS design if effective dimensions can be found using a smaller grid, e.g. the $28\times24$ grid in case 2, to model the FSS in varied dielectric and/or stacked configurations (see below).

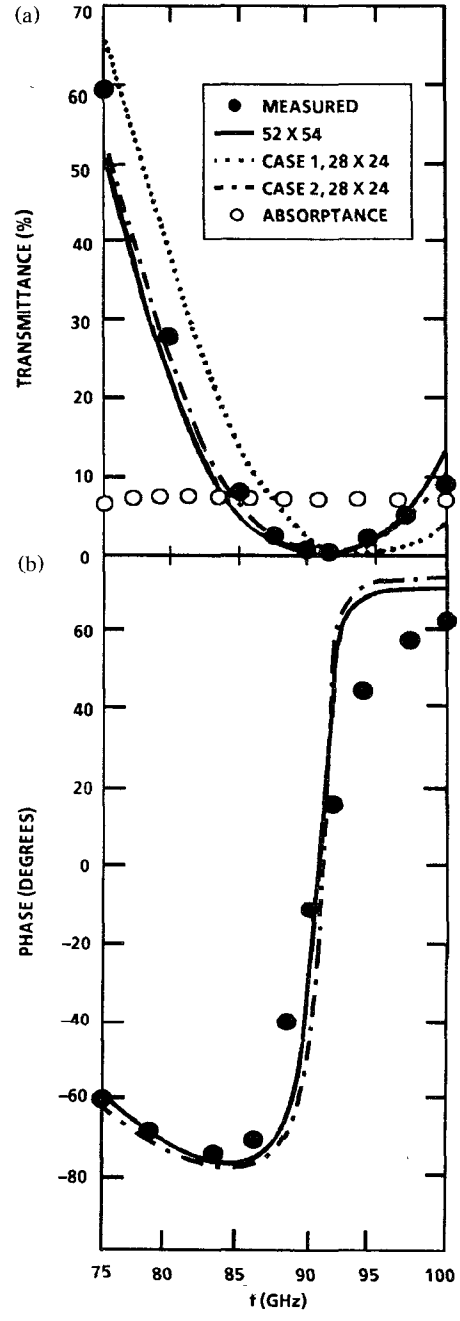


Fig. 4. Aluminum I-pole array results: (a) Measured (•) and predicted transmittance for three different grid solutions, and predicted absorptance (○). (b) Measured (•) and predicted phase results, for the $52\times54$ and case 2, $28\times24$ grids.

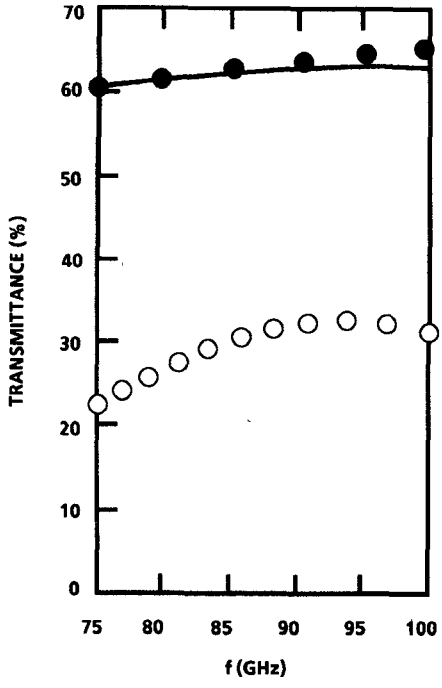


Fig. 5. Bismuth I-pole results: measured (•) and predicted (solid line) transmittance and predicted absorptance (○).

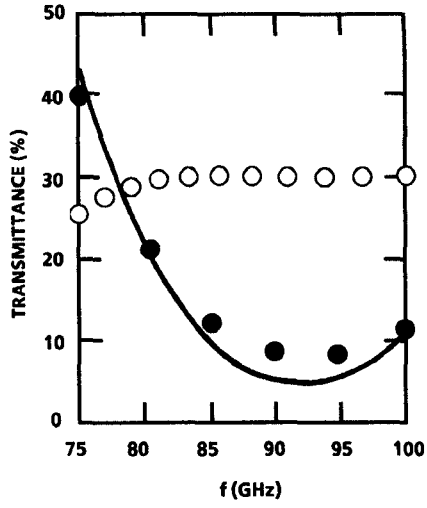


Fig. 6. Bismuth-loaded aluminum I-pole results: measured (•) and predicted (solid line) transmittance and predicted absorptance (○).

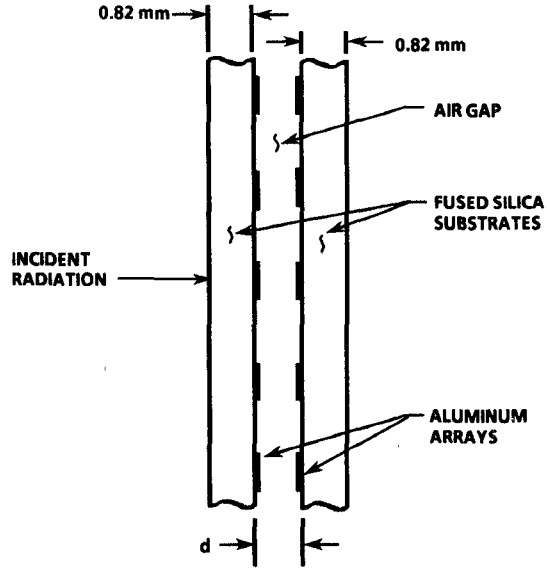


Fig. 7. Doubly stacked aluminum I-pole array geometry.

The predicted absorptance for the 52×54 grid is also shown in Fig. 4(a). It is essentially flat across the band, with an average value of ~7%. The results of the transmission phase measurement are shown in Fig. 4(b). Phase predictions were obtained using the 52×54 grid and the 28×24 grid in case 2 for the numerical analysis.

The transmittance of a 1500-Å-thick bismuth I-pole array is shown in Fig. 5, with excellent agreement between simulation and experiment. An average absorptance of ~30% is predicted across the band with a broad peak centered at ~94 GHz. The 52×54 resolution grid was used for the simulation. The measured sheet conductance of the bismuth film was 0.024 $(\Omega/\text{square})^{-1}$. Since the estimated skin depth far exceeds the film thickness, a dc measurement of sheet conductance was used for the numerical analysis.

The transmittance and predicted absorptance for the bismuth-loaded I-pole array (Fig. 3(b)) are shown in Fig. 6. The results were obtained using a 52×54 grid with an average of 470 iterations required for convergence to within 1% error. The large number of iterations indicates that direct matrix inversion might be more efficient in modeling this structure [15], [20].

The cascaded aluminum arrays in Fig. 7 are separated by distance $d$. The scattering matrix elements are not equal for the two arrays because the substrates are respectively in front of and behind the FSS. This allowed the separation distance to be made small enough so that the effect of first-order evanescent Floquet mode coupling could be studied.

The transmittance and predicted absorptance for various separation distances are shown in Fig. 8. In Fig. 8(a), $d = 0.2$ mm, and the transmittance exhibits a band-stop characteristic with the band edge at ~86 GHz. At this separation, the evanescent $(\pm 1, 0)$ and $(0, \pm 1)$ first-order diffractive mode couplings are large and are included in the cascade analysis. Evidence of this is a discrepancy in the band edge observed when these higher order terms are ignored, while the correct band edge is predicted when the terms are included (although a discrepancy is observed at lower frequencies). The scattering matrix elements were calculated using a 28×24 grid and the case 2 modeling dimensions given in Table I. This considerably reduced the computer time required to calculate the scattering matrices (including first-order modes) compared with use of the 52×54 grid.

Results for the $d = 0.4$ mm separation are shown in Fig. 8(b). At this separation the evanescent-mode couplings are small enough to be ignored. The transmittance exhibits a band-stop with the band edge at ~79 GHz. Results for the 28×24 grid of case 2 and the 52×54 grid are shown. Both are in close agreement with experiment. Results are essentially the same when the first-order diffractive modes are included. Finally, the results for $d = 0.8$ mm separation are shown in Fig. 8(c).

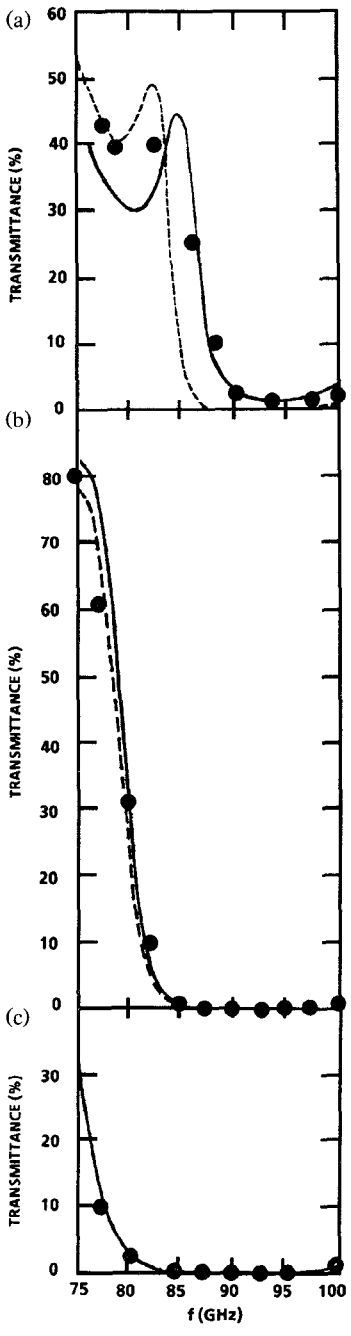


Fig. 8. Doubly stacked aluminum I-pole array results. (a) Measured (•) and predicted transmittance with first-order Floquet modes (solid line) and (0,0) mode only (dashed line) for $d = 0.2$ mm. (b) $d = 0.4$ mm results for measured transmittance (•), case 2 $28\times24$ grid (solid line), and $52\times54$ grid (dashed line). (c) $d = 0.8$ mm results.

## V. Conclusion

The purpose of this investigation was a comparative study of numerical and experimental results for the W-band frequency selective properties of various arrays.

The numerical method used to describe scattering from a dielectric-mounted FSS has been previously discussed [14], [15]. The most general dielectric configuration considered involved an FSS sandwiched between (lossy) dielectric layers together with a lossless superstrate and (lossy) substrate. The electric field integral equation was obtained using rooftop subdomain basis and testing functions within the framework of the Galerkin testing procedure and is applicable to the general case of an arbitrarily shaped FSS consisting of multiple lossy and/or reactive materials. The resulting operator equation was solved iteratively using the conjugate gradient method. We have addressed scattering from stacked FSS's using the cascade approach. The immediately adjacent dielectric layers are included in the construction of the FSS scattering matrix, thus reducing the size of the scattering matrix necessary to obtain accurate results for stacked FSS's/dielectric layers within the framework of the cascade connection.

The results presented for the aluminum, bismuth, and bismuth-loaded I-pole arrays on fused silica included spectral transmittance measurements and predictions together with predicted spectral absorptance. To accurately model the I-pole arrays, a large $(52\times54)$ grid was used to discretize the unit cell. Very good agreement was found between theory and experiment in all cases. The use of effective dimensions and a smaller $(28\times24)$ unit cell grid size was also investigated for the case of the aluminum array in an effort to reduce CPU requirements. Excellent agreement with experiment was observed if the I-pole width parameters were made larger than the measured values.

Results for transmittance through a pair of stacked aluminum I-pole arrays mounted on fused silica were also obtained, with excellent agreement between theory and experiment observed for three separation distances between the two arrays. The cascaded arrays exhibited a band-stop characteristic in W-band. At the smallest separation the effect of the first-order evanescent Floquet modes on the position of the band edge was observed. The inclusion of these models leads to a correct prediction for the band edge. In constructing the scattering matrix for this case the smaller $(28\times24)$ grid size was used to significantly reduce computer time. For the larger separation distances, for which only the lowest order (0,0) mode was needed in the scattering matrix, the results for both the $28\times24$ and $52\times54$ grid sizes were analyzed and found to be in excellent agreement with experiment.

## Appendix
## Sheet Conductances of Thin Mesh Films

To accurately simulate scattering by the numerical method described in this paper, the thickness, $t$, of the frequency selective surface must be small, $t \ll \lambda$. The materials in the FSS can then be approximated by films of infinitesimal thickness and specified sheet conductance. The sheet conductance will be derived by first considering Fig. 9, which shows a continuous film that is not an FSS. The film is characterized by a complex index of refraction, $\hat{N} = N - jK$, from which one can obtain the complex conductivity, $\hat{\sigma} = \sigma_1 + j\sigma_2 = j\omega\epsilon_0(\hat{N})^2$; the intrinsic admittance, $\hat{Y} = (1/377)\hat{N}$; and the propagation constant, $\hat{\gamma} = j(2\pi/\lambda)\hat{N}$.

At the input and output surfaces, the complex electric and magnetic fields are represented by $E_{IN}, H_{IN}$ and $E_R, H_R$ respectively. $E_{IN}$ and $H_{IN}$ are the sums of the incident and reflected fields. The admittance of free space to the right of the film is $Y_R = H_R/E_R = 1/377(\Omega)^{-1}$. The film admittance including the effect of the right-hand half-space is $\hat{Y}_{IN} = H_{IN}/E_{IN}$. However, the desired sheet conductance is $\hat{\sigma}_S = H_F/E_{IN}(\Omega/\text{square})^{-1}$, where $H_F$ is the contribution to the magnetic field at the input due to the conduction and dis-

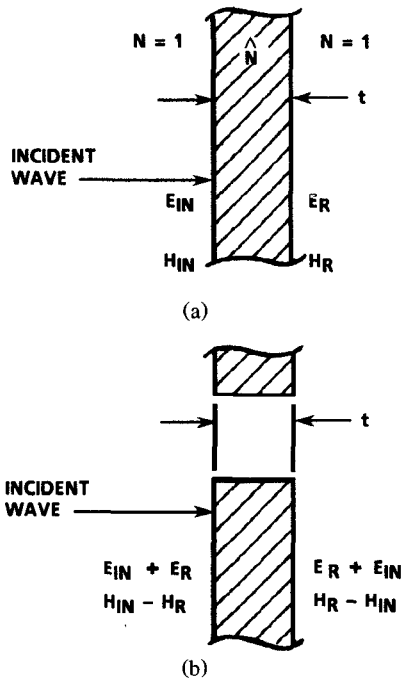


Fig. 9. Boundary conditions on (a) continuous and (b) mesh films.

placement current in the film only:

$$\hat{\sigma}_S = \frac{H_F}{E_{IN}} = \frac{H_{IN} - H_R}{E_{IN}} = \hat{Y}_{IN} - \frac{E_R}{E_{IN}} Y_R.$$

The quantity $\hat{\sigma}_S$ can be obtained by solving the Maxwell–Ampere integral equation for $H_F$ or by simply applying well-known transmission line equations [28]:

$$\hat{Y}_{IN} = \hat{Y} \frac{\cosh \hat{\gamma} t + \hat{N} \sinh \hat{\gamma} t}{\hat{N} \cosh \hat{\gamma} t + \sinh \hat{\gamma} t} \tag{A1}$$

$$\frac{E_R}{E_{IN}} = \frac{\hat{N}}{\hat{N} \cosh \hat{\gamma} t + \sinh \hat{\gamma} t} \tag{A2}$$

$$\hat{\sigma}_S = \hat{Y} \frac{\cosh \hat{\gamma} t + \hat{N} \sinh \hat{\gamma} t - 1}{\hat{N} \cosh \hat{\gamma} t + \sinh \hat{\gamma} t}. \tag{A3}$$

Because of the open areas in the thin FSS described in this paper, the electric field is impressed nearly equally on both sides of the film. Applying superposition as shown in Fig. 9(b), the current in the film is doubled and the sheet conductance, $\hat{\sigma}_{SS}$, is given by

$$\hat{\sigma}_{SS} = \frac{2H_F}{E_{IN} + E_R} = \frac{2\hat{\sigma}_S}{1 + (E_R / E_{IN})}$$

$$= 2\hat{Y} \frac{\cosh \hat{\gamma} t + \hat{N} \sinh \hat{\gamma} t - 1}{\hat{N} \cosh \hat{\gamma} t + \sinh \hat{\gamma} t + \hat{N}}. \tag{A4}$$

If the film thickness is much smaller or larger than the skin depth, $\hat{\delta} = \lambda / 2\pi K$, $\hat{\sigma}_{SS}$ reduces to

$$\hat{\sigma}_{SS} \sim \hat{\sigma} t \qquad (t \ll \delta)$$

and

$$\hat{\sigma}_{SS} \sim \hat{2}Y \qquad (t \gg \delta).$$

## Acknowledgment

The authors express their gratitude to J. Smotherman for help in device fabrication and to G. Clardy and T. Shafer for device testing and technical assistance. They also thank W. E. Case for helpful discussions.

## References

[1] G. D. Holah, and J. P. Auton, "Interference filters for the far infrared," *Infrared Phys.*, vol. 14, pp. 217–229, 1974.
[2] R. Ulrich, "Effective low-pass filters for far infrared frequencies," *Infrared Phys.*, vol. 7, pp. 65–74, 1967.
[3] S. T. Chase, and R. D. Joseph, "Resonant array bandpass filter for the far infrared," *Appl. Opt.*, vol. 22, pp. 1775–1779, 1983.
[4] E. J. Danielewicz and P. D. Coleman, "Hybrid metal mesh dielectric mirrors for optically pumped far infrared lasers," *Appl. Opt.*, vol. 15, pp. 761–767, 1976.
[5] D. A. Weitz, W. J. Skocpol, and M. Tinkham, "Capacitive-mesh output couplers for optically pumped far-infrared lasers," *Opt. Lett.*, vol. 3, pp. 13–15, 1978.
[6] R. Ulrich, T. J. Bridges, and M. A. Pollock, "Variable metal mesh coupler for far infrared lasers," *Appl. Opt.*, vol. 9, pp. 2511–2516, 1970.
[7] P. F. Goldsmith, in *Infrared and Millimeter Waves*, vol. 6, K. J. Button, Ed. New York: Academic Press, 1982, pp. 277–343.
[8] J. A. Araud and J. T. Ruscio, "Resonant-grid quasioptical diplexer," *Bell Syst. Tech. J.*, vol. 54, pp. 263–283, 1975.
[9] R. Ulrich, K. F. Renk, and L. Gerzel, "Tunable submillimeter interferometers of the Fabry–Perot Type," *IEEE Trans. Microwave Theory Tech.*, vol. MTT-11, pp. 363–371, 1963.
[10] D. B. Rutledge and S. E. Schwarz, "Planar multimode detector arrays for infrared and millimeter-wave applications," *IEEE J. Quantum Electron.*, vol. QE-17, pp. 407–414, 1981.
[11] A. J. Brouns, "A new concept for a phased array antenna at millimeter wavelengths," Final Tech. Rep., Air Force Contract F08635-85-C-0273, Rep. No. AFATL TR 88-80, Nov. 1987.
[12] W. W. Lam *et al.*, "Millimeter-wave diode-grid phase shifters," *IEEE Trans. Microwave Theory Tech.*, vol. 36, pp. 902–907, 1988.
[13] C. F. Jou *et al.*, "Millimeter-wave diode-grid frequency doubler," *IEEE Trans. Microwave Theory Tech.*, vol. 36, pp. 1507–1514, 1988.
[14] T. Schimert, M. E. Koch, and C. H. Chan, "Analysis of scattering from frequency selective surfaces in the infrared," *J. Opt. Soc. Amer. A*, vol. 7, pp. 1545–1553, Aug. 1990.
[15] R. Mittra, C. H. Chan, and T. Cwik, "Techniques for analyzing frequency selective surfaces—a review," *Proc. IEEE*, vol. 76, pp. 1593–1615, 1988.
[16] B. J. Rubin and H. L. Bertoni, "Reflection from a periodically perforated plane using a subsectional current approximation," *IEEE Trans. Antennas Propagat.*, vol. AP-31, pp. 829–836, 1983.
[17] T. Cwik and R. Mittra, "Scattering from a periodic array of free-standing arbitrarily shaped perfectly conducting or resistive patches," *IEEE Trans. Antennas Propagat.*, vol. AP-35, pp. 1226–1234, 1987.
[18] C. H. Chan, "Investigation of iterative and spectral Galerkin techniques for solving electromagnetic boundary values problems," Ph.D. dissertation, Univ. Illinois, Urbana, 1987.
[19] J. P. Montgomery and K. R. Davey, "The solution of planar periodic structures using iterative methods," *Electromagnetics*, vol. 5, pp. 209–235, 1985.
[20] C. H. Chan, "A numerically efficient technique for the method of moments solution of electromagnetic problem associated with planar periodic structures," *Microwave and Opt. Technol. Lett.*, vol. 1, pp. 372–374, 1988.
[21] T. Cwik and R. Mittra, "Scattering from general periodic screens," *Electromagnetics*, vol. 5, pp. 263–283, 1985.
[22] T. Cwik and R. Mittra, "The cascade connection of planar periodic surfaces and lossy dielectric layers to form an arbitrary periodic screen," *IEEE Trans. Antennas Propagat.*, vol. AP-35, pp. 1397–1405, 1987.
[23] T. Cwik and R. Mittra, "Correction to 'The cascade connection of planar periodic surfaces and lossy dielectric layers to form

an arbitrary periodic screen'," *IEEE Trans. Antennas Propagat.*, vol. 36, p. 1335, 1988.
[24] S. Contu and R. Tascone, "Scattering from passive arrays in plane stratified regions," *Electromagnetics*, vol. 5, pp. 285–306, 1985.
[25] R. J. Luebbers and B. A. Munk, "Mode matching analysis of biplanar slot arrays," *IEEE Trans. Antennas Propagat.*, vol. AP-27, pp. 441–443, 1979.
[26] B. A. Munk and T. W. Kornbau, "On the stabilization of the bandwidth of a dichroic surface by use of dielectric slabs," *Electromagnetics*, vol. 5, pp. 349–373, 1985.
[27] M. A. Ordal *et al.*, "Optical properties of the metals Al, Co, Cu, An, Fe, Pb, Ni, Pd, Pt, Ag, Ti and W in the infrared and far infrared," *Appl. Opt.*, vol. 22, pp. 1099–1119, 1983.
[28] W. C. Johnson, *Transmission Lines and Networks*. New York: McGraw-Hill, 1950, p. 105.

✠

**Thomas R. Schimert** (A'87), photograph and biography not available at the time of publication.

✠

**Austin J. Brouns** (SM'70), photograph and biography not available at the time of publication.

**Chi H. Chan** (S'86–M'86), photograph and biography not available at the time of publication.

✠

**Raj Mittra** (S'54–M'57–SM'69–F'71) is Director of the Electromagnetic Communication Laboratory of the Electrical and Computer Engineering Department and Research Professor of the Coordinated Science Laboratory at the University of Illinois. He is a former president of AP-S, and he has served as the editor of the IEEE TRANSACTIONS ON ANTENNAS AND PROPAGATION. He is president of RM Associates, a consulting organization providing services to several industrial and governmental organizations.

Dr. Mittra's professional interests include the areas of analytical and computer-aided electromagnetics, high-speed digital circuits, radar scattering, satellite antennas, microwave and millimeter-wave integrated circuits, frequency selective surfaces, EMP and EMC analysis, and remote sensing.